

Synergy of Cu-Mn bimetallics under nano-confined catalysis in a membrane-based peroxyomonosulfate system



Yangli Cui ^{a,b}, Wenjie Gao ^b, Wenchao Peng ^c, Eslam Salama ^d, Mona Ossman ^d, Lan Liang ^b, Xu He ^b, Beibei Yan ^b, Ning Li ^{b,*}, Guanyi Chen ^{a,b,e,*}

^a School of Ecology and Environment, Tibet University/Key Laboratory of Plateau Environmental Engineering and Pollution Control, Lhasa 850000, PR China

^b School of Environmental Science and Engineering, Tianjin University/Tianjin Key Lab of Biomass/Wastes Utilization, Tianjin 300072, PR China

^c Department of Chemical Engineering, Tianjin University, Tianjin 300350, PR China

^d Environment and Natural Materials Research Institute (ENMRI), City of Scientific Research and Technological Applications (SRTA-City), New Borg El-Arab City, Alexandria 21934, Egypt

^e School of Mechanical Engineering, Tianjin University of Commerce, Tianjin 300134, PR China

ARTICLE INFO

Keywords:

Bimetallic synergy
Nano-confine
Electronic coupling
Membrane
Advanced oxidation

ABSTRACT

The electronic interactions of bimetals were investigated in the confined membrane environment. In this work, Cu-Mn oxides were loaded on polytetrafluoroethylene (PTFE) membrane surface for nano-confined PMS activation and sulfamethoxazole (SMX) degradation. The CuO@MnO₂/PTFE membrane achieved SMX removal with constant of 0.1268 min⁻¹ in PMS system, which was higher than that in traditional advanced oxidation process (0.0949 min⁻¹). The confined Cu and Mn sites enhanced electronic coupling, which promoted the electron rearrangement of metal sites and facilitated PMS adsorption and activation. As a result, SO₄²⁻ (48.11%) and *OH (31.78%) played a dominant role in CuO@MnO₂/PTFE membrane/PMS system, hence achieving faster removal of SMX. The obtained results help to understand the PMS activation process with confined bimetals, which ultimately promotes the development and application of confined catalysis.

1. Introduction

Sulfamethoxazole (SMX) has increasingly appeared in wastewater due to wide applications. The robust stability and antimicrobial activity may lead to the development of resistant bacteria and resistance genes, posing potential threats to human health and ecological safety [1]. The concentration of SMX in pharmaceutical wastewater could reach 27.9 mg/L [2], while only about 52% of SMX can be removed by secondary treatment in wastewater treatment plants [3]. Advanced oxidation technologies (AOPs) were effective for the removal of organic pollutants from water, especially persulfate (PS)-based AOPs owing to broader pH adaptability, higher redox potential and longer half-life of active species [4]. Comparatively, peroxyomonosulfate (PMS) was regarded with high reactivity due to asymmetric structure and extended O-O bond [5].

Metal-based heterogeneous catalysts such as transitional metals, metal oxides and metal composites have been used to activate PMS [6]. Copper (Cu) and manganese (Mn)-based catalysts were promising owing to low toxicity, easy accessibility and eco-friendliness. Both have been

widely applied for organic pollutant degradation in a PS activation by radical and non-radical pathways individually or compositely [7,8]. In recent years, the mechanism of bimetallic synergistic activation of PS had been extensively studied. Primarily, compared with monometallic, bimetallic increased the reactive sites and promoted the adsorption of oxygen-containing substances [9]. Moreover, the synergistic redox of different metals facilitated PMS activation [10]. In addition, some metals could increase oxygen vacancies by constructing connections between bimetals and O and ultimately accelerating the generation of ROS [11]. Furthermore, electronic coupling between bimetallic atoms could adjust electron capture from pollutants and adsorption strength for PMS, hence establishing electron transport channels and facilitating electronic rearrangement [12,13]. Subsequently, electrons were captured by PMS adsorption, resulting in ROS formation for pollutant degradation [14].

However, traditional powder catalysts face challenges of recycling and ineffective utilization of active sites due to agglomeration. Loading catalysts on membranes provided an efficient solution, which could form a nano-confined environment (preferably < 25 nm) [15,16].

* Correspondence to: No.135, Yaguan Road, Jinnan District, Tianjin City, PR China.

E-mail addresses: liningec@tju.edu.cn (N. Li), chen@tju.edu.cn (G. Chen).

Meanwhile, the confined catalytic membrane was superior to the conventional unconfined heterogeneous one in terms of activating PMS for pollutant degradation. It is attributed to the easier enrichment of contaminants and efficient electron transfer between the catalyst and target contaminants in the nano-confined environment [17–19].

Besides, several studies reported nanoconfined catalysts in AOP to achieve efficient removal of pollutants [20,21]. For example, Xu et al. doped Co-Fe atomic pairs in metal-organic frameworks to obtain confined catalysts. The electronic interactions of atomic pairs catalyst could reduce the secondary energy barrier for electrons transfer from contaminant to catalyst, and subsequently to PMS [22,23]. Further, the corresponding reaction rate constant k (2.06 min^{-1}) of bisphenol A was 5.1 times higher than that of the single atom catalyst [23]. Noticeably, bimetallic catalysts were easier to recover under confined membrane environment, which had greater potential for application than confined catalysts. Sufficient contact of contaminants, oxidants and catalysts [18, 19] might accelerate the generation of ROS through confined membrane during continuous filtration. However, to the best of our knowledge, the mechanism of bimetallic catalysts activation has not yet been studied in a confined membrane environment.

In this study, the PTFE membrane was selected as a substrate due to extreme stability. Moreover, the confined environment was constructed by CuO@MnO₂/PTFE membranes preparation for SMX removal in a PMS system. Additionally, the morphology and chemical composition of the prepared membrane were investigated. The mechanism of PMS activation and nano-confined oxidization was also illustrated by experimental and DFT theoretical calculations. This work enriches the mechanism of nano-confined oxidization and bimetallic catalytic synergies to provide novel insights for the efficient removal of contaminants from water.

2. Experimental

2.1. Materials and reagents

All chemical reagents were analytical grade and the details were given in the Text S1 of [Supporting Information \(SI\)](#).

2.2. Characterizations

The chemical composition and morphology characterization of catalysts and catalytic membranes were conducted by X-ray diffraction (XRD), X-ray photoelectron spectroscopy (XPS), Fourier transform infrared (FTIR), scanning electron microscopy (SEM) and transmission electron microscopy (TEM). Additionally, catalyst electronegativity was determined by zeta potential meter. The hydrophilicity of the membrane was measured by contact angle meter (CA). Further, the physical properties of catalysts and pore size distribution of catalytic membranes were obtained via Brunauer-Emmett-Teller (BET). Besides, SMX and reaction product of SMX were analyzed by high performance liquid chromatography (HPLC) and high-performance liquid chromatography mass spectrometry (LC-MS), respectively. Moreover, metals leached during the reaction can be determined by inductively coupled plasma mass spectrometry (ICP-MS). And the leached metals and produced reactive species during the reaction can be detected by ICP-MS and electron paramagnetic resonance (EPR), respectively. Details of the above test methods were provided in Text S2 of SI.

2.3. Preparation of catalysts and catalytic membranes

CuO@MnO₂ and MnO₂ were prepared by a simple single-step reflux method. Afterward, the catalytic membranes were obtained by vacuum-assisted filtration. The detailed preparation procedure was listed in Text S3 of SI.

2.4. Membrane filtration experiment

The total injection volume for each experiment was 100 mL in the filtration process. The influent side was a mixture of contaminant (15 mg/L) and PMS, driven by the pumping pressure of the peristaltic pump rotation. The water through membrane was collected and filtrate the mass was weighed on scales. Further, the produced water was poured back to the influent after an interval for recirculation and filtration. The water produced was withdrawn by syringe at 10 min intervals and added to a liquid phase vial containing an excess of Na₂S₂O₃. The procedure for the circular filtration experiment was listed in Text S4. In addition, ROSSs were identified by quenching experiments, and the details were listed in Text S5 Calculations of membrane filtration performance metrics were displayed in Text S6 of SI.

2.5. DFT calculations

The structure optimization of confined CuO@MnO₂/PTFE membrane and unconfined CuO@MnO₂ powder were conducted by density functional theory (DFT). Additionally, DFT calculations were applied in the adsorptive configuration of PMS on the catalyst and the Crystal Orbital Hamilton Population (COHP) between the metal active sites of the catalyst. The details were shown in Text S7 of SI.

3. Results and discussion

3.1. Characterization of CuO@MnO₂ and CuO@MnO₂/PTFE membrane

3.1.1. Chemical composition

The composition and morphology of the prepared catalysts and catalytic membranes were evaluated with results shown in [Fig. 1](#). XRD patterns of the prepared catalysts and membranes were depicted in [Fig. 1\(a\)](#). The peaks at 12.68°, 17.98°, 28.74°, 37.52°, 41.94°, 49.82°, 60.16°, and 65.38° were identified as the (110), (200), (310), (121), (301), (411), (521) and (002) planes of α-MnO₂ (JC PDF No. 72–1982), respectively [24]. The crystal planes confirmed that MnO₂ had been successfully synthesized. However, no obvious change was found in CuO@MnO₂ composites compared with MnO₂, which may be due to the relatively low loading of Cu [25]. Besides, the peaks of the original membrane were assigned to PTFE (JC PDF No. 54–1594) [26]. The PTFE characteristic peaks of CuO@MnO₂/PTFE membrane became weak, which was mainly attributed to the deposition of CuO@MnO₂, covering the signals of the PTFE substrate. The above results indicated the successful preparation of CuO@MnO₂/PTFE membrane.

The elemental compositions and valence states of MnO₂ and CuO@MnO₂ composites were further provided by XPS spectroscopy in [Fig. 1\(b-d\)](#). Obviously, the existence of O and Mn elements was confirmed by the XPS survey spectra of MnO₂ and CuO@MnO₂. In addition, weak Cu peaks were observed in the XPS spectra of CuO@MnO₂. The Mn2p XPS spectrum ([Fig. S4\(a\)](#)) of CuO@MnO₂ showed two peaks at binding energies of 653.89 and 642.22 eV, corresponding to the Mn2p_{1/2} and Mn2p_{3/2} respectively. A satellite peak with a binding energy of 665.20 eV was observed, which was compatible with the typical MnO₂ characteristic peak [27,28]. The Mn2p_{3/2} ([Fig. 1\(c\)](#)) was divided into three peaks at 642.15, 642.41, and 644.48 eV, which were assigned to the Mn(II), Mn(III) and Mn(IV), respectively. The presence of Mn(III) could promote the generation of oxygen vacancies (O_v) due to electrostatic equilibrium [29]. Hence, the higher ratio of the Mn(III)/Mn(IV) was associated with higher O_v content. Obviously, the value of Mn(III)/Mn(IV) (6.84) after Cu doping was greater than that of undoped MnO₂ (4.80), indicating that more Mn(III) was available in CuO@MnO₂. Increased Mn(III) content led to the generation of more O defects [30,31]. Hence, O was released more easily, which could improve the catalytic performance [32]. In addition, the Cu 2p_{3/2} of CuO@MnO₂ ([Fig. 1\(d\)](#)) showed a binding energy of 933.34 eV, revealing the existence of CuO in the Cu@MnO₂ composite

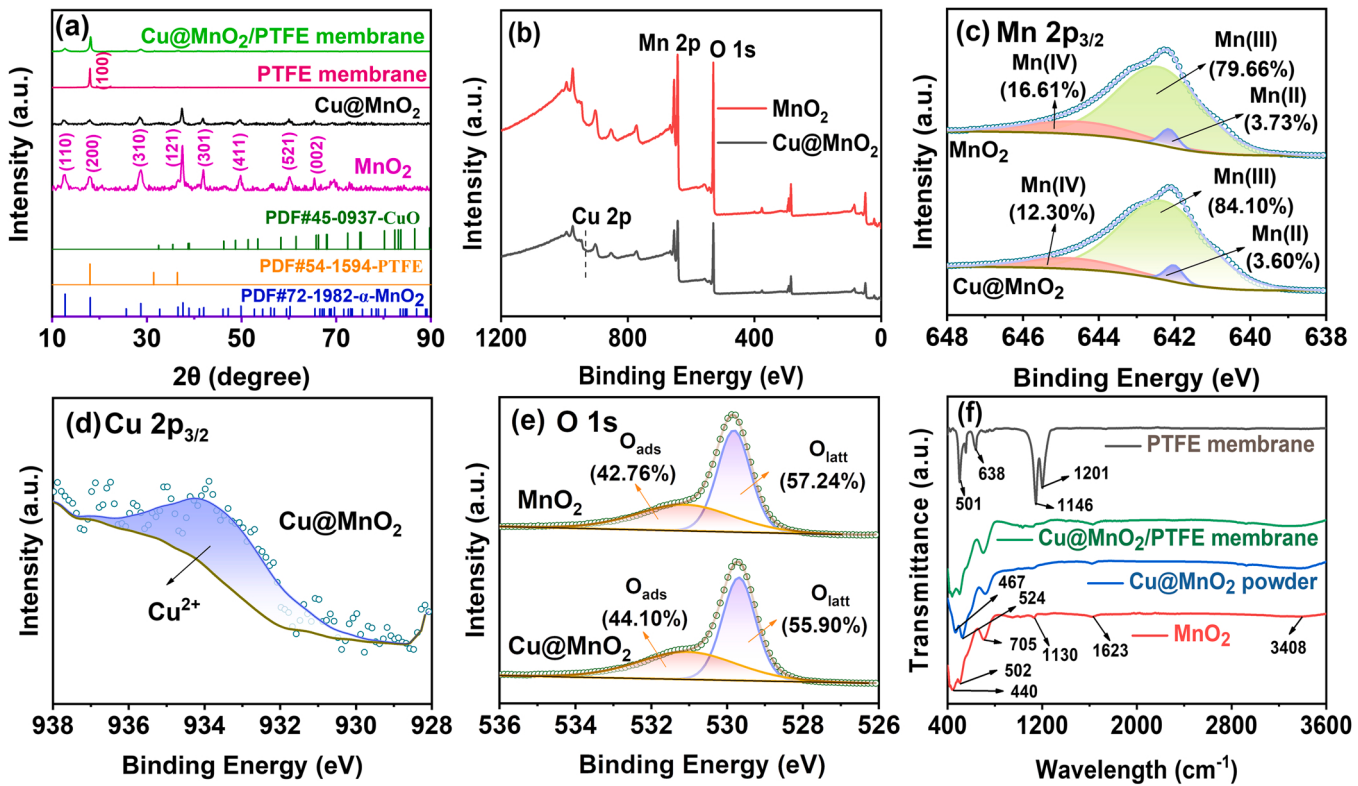


Fig. 1. (a) XRD patterns of different samples; (b) XPS survey and high-resolution XPS spectra of (c) Mn 2p_{3/2}, (d) Cu 2p_{3/2} and (e) O 1s; (f) FTIR spectra of the prepared powder and membrane samples.

[33,34]. The XPS-O1s spectra were shown in Fig. 1(e). The O1s of MnO₂ could be divided into two peaks at 529.82 eV (57.24%) and 531.12 eV (42.76%), corresponding to the surface lattice oxygen (O_{latt}) and adsorbed oxygen (O_{ads}), respectively [35]. Since oxygen molecules can be adsorbed on O_v and converted to O_{ads} on the catalyst surface, the O_{ads}/O_{latt} ratio can represent the amount of O_v [36]. The O_{ads}/O_{latt} value of CuO@MnO₂ (0.79) was higher than that of MnO₂ (0.75), suggesting that Cu doping led to the appearance of more O_v. As a result, the structural distortion of the catalyst occurred, favoring the release of lattice oxygen from the catalyst surface [37].

The functional groups in catalysts and catalytic membranes were further monitored by FTIR (Fig. 1(f)). As for MnO₂, the peak near 3408 cm⁻¹ matched with the stretching vibration of hydroxyl groups, while the peaks around 1130 and 1623 cm⁻¹ represented the bending vibrations of -OH groups and surface-adsorbed H₂O molecules, respectively [35]. Moreover, several peaks at around 440, 502 and 705 cm⁻¹ were associated with lattice vibrations of Mn-O bonds [38,39]. As for CuO@MnO₂ surface, the stretching vibrations at 467 and 524 cm⁻¹ were attributed to Cu-O bonds [40,41]. Besides, the intense peaks at 1146 and 1201 cm⁻¹ on the PTFE membrane were assigned to the symmetric and asymmetric stretching of CF₂ groups [42]. Additionally, the peaks near 501 and 638 cm⁻¹ were related to the deformation and rocking vibration modes of CF₂ [43]. Thus, the results further validated the successful preparation of the CuO@MnO₂/PTFE membrane.

3.1.2. Morphology

Fig. 2 showed the surface morphology of the catalyst and catalytic membrane via SEM and TEM. As presented in Fig. 2(a), the pristine PTFE membrane exhibited a porous and smooth fiber structure. As can be seen from the image of CuO@MnO₂/PTFE membrane, the CuO@MnO₂ was uniformly distributed on the surface of the PTFE membrane. Further, the content of Cu elements was detected as approximately 1.42%. By comparing Fig. 2(b) with Fig. S4(b), both MnO₂ and CuO@MnO₂ on the PTFE membrane primarily showed nanorod structures. Additionally, the

MnO₂ was slenderer. The average length and diameter of MnO₂ nanorods were approximately 240 and 30 nm, respectively, smaller than those of CuO@MnO₂ (average length of 275 nm and diameter of 57 nm). Moreover, MnO₂ tended to aggregate, leading to uneven dispersion.

Besides, TEM were further conducted to identify the microstructures of CuO@MnO₂. As seen in Fig. 2(c-d), the crystal facets (310), (121), and (301) belonging to MnO₂ were observed, which compatible with the XRD. Additionally, mapping images of CuO@MnO₂ (Fig. S5(a)-(d)) confirmed uniform distribution of CuO in the catalyst. The above results demonstrating CuO was uniformly doped on the surface of MnO₂, hence improving the structure and dispersion. Additionally, the surface area and pore volume of CuO@MnO₂ were larger than those of MnO₂ (Text S8), demonstrating the improvement of catalyst structure by Cu doping. The CuO@MnO₂ exhibited positive charge under acidic conditions while showing negative charge under neutral to alkaline conditions (Text S9 and Fig. S6). Furthermore, the contact angle results confirmed the high hydrophilicity of the CuO@MnO₂/PTFE membrane and MnO₂/PTFE membrane (Text S9).

3.2. SMX removal by CuO@MnO₂/PTFE membrane/PMS system

3.2.1. Influencing factors on SMX removal

As shown in Fig. S7, PEG was not involved in the SMX degradation (Text 10). To further investigate the impact of reaction conditions on SMX removal, the PMS concentration, pH, and the loading of CuO@MnO₂ on the PTFE membrane were optimized, and the results were displayed in Fig. 3. The influence of the PMS concentration on the filtration process was shown in Fig. 3(a) and 3(d). Obviously, the catalyst could hardly adsorb SMX without PMS. While the removal rate of SMX ranged from 63.7% to 98.9% within 60 min as the PMS concentration increased from 0.5 to 1.5 mM. The lower removal rate of SMX under low concentration of PMS was mainly attributed to the insufficient contact of PMS molecules with catalyst sites. Increasing the PMS concentration produced more ROS to react with SMX, resulting in higher

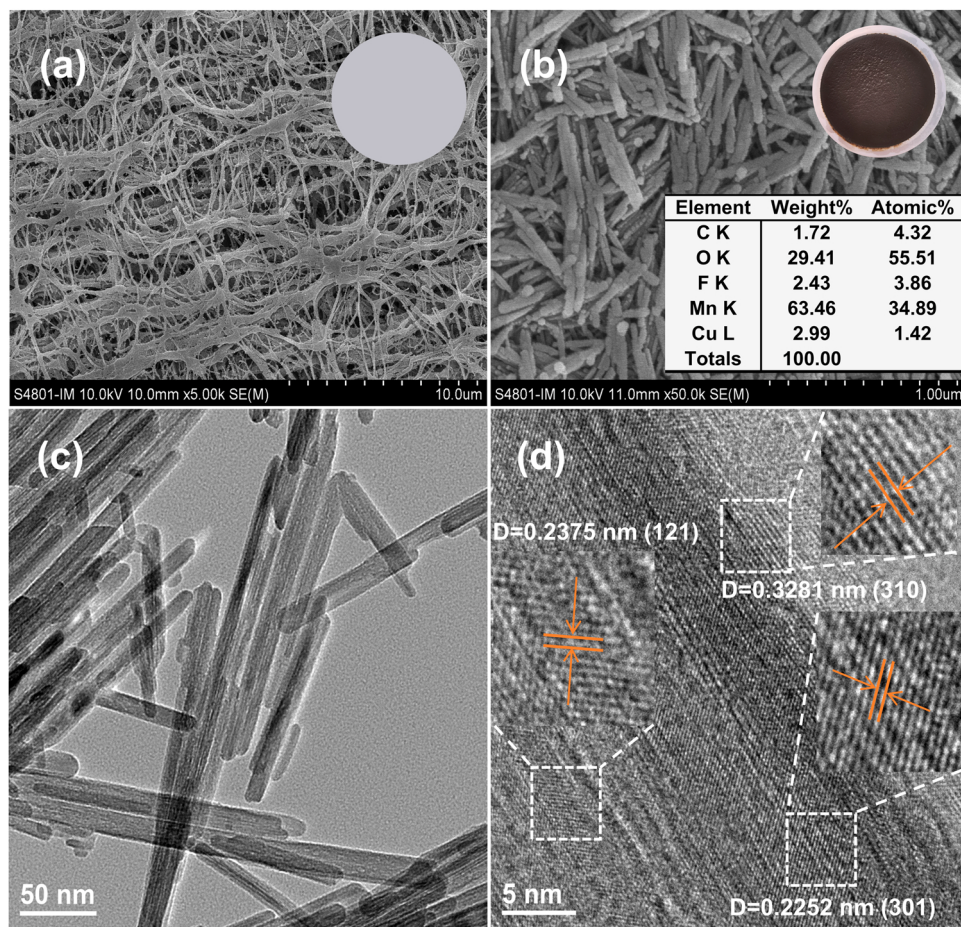


Fig. 2. SEM images of (a) PTFE membrane and (b) CuO@MnO₂/PTFE membrane; (c)-(d) TEM images of CuO@MnO₂.

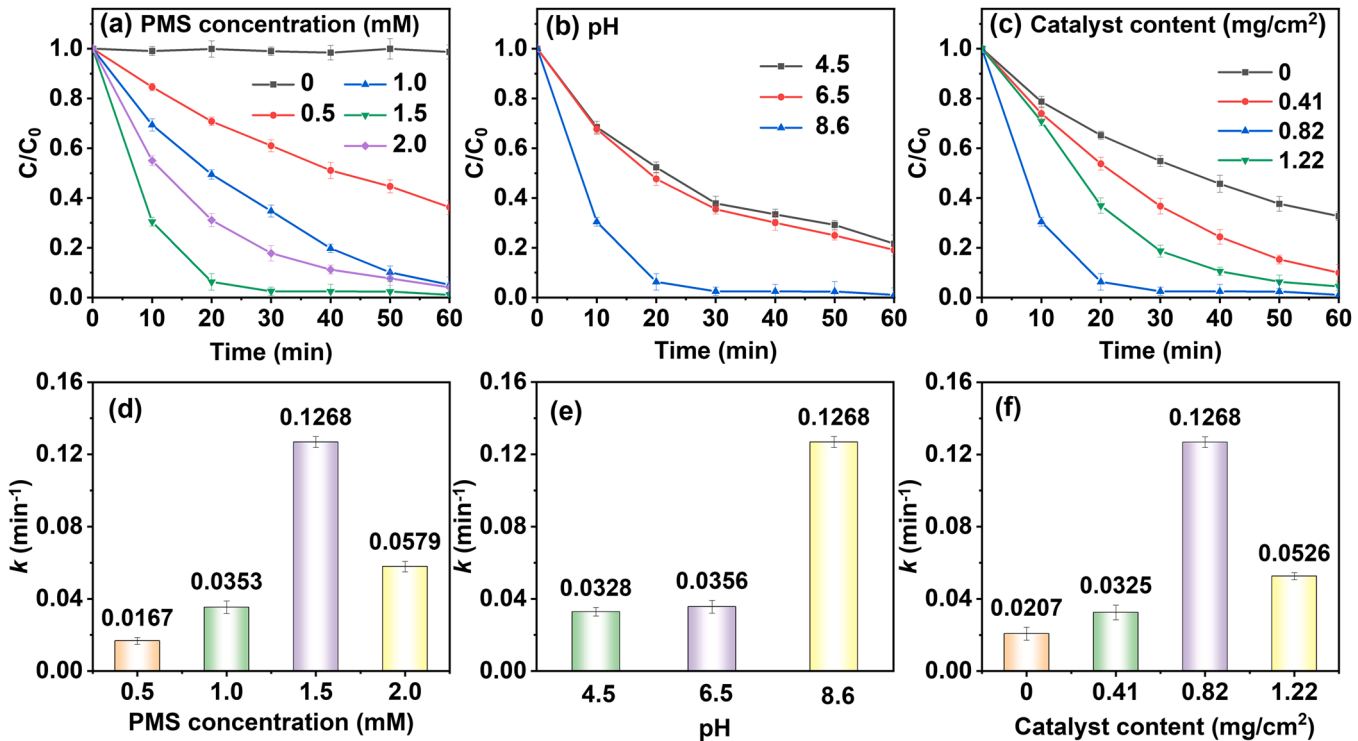
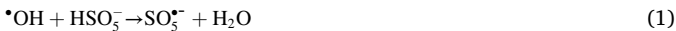


Fig. 3. Removal of SMX with different (a) PMS concentrations, (b) pH, (c) catalyst contents on PTFE membrane surface and (d-f) corresponding apparent rate constants (k). $C_0(\text{SMX}) = 15 \text{ mg/L}$, $[\text{PMS}] = 1.5 \text{ mM}$, $\text{pH} = 8.6$, $C(\text{CuO@MnO}_2) = 0.82 \text{ mg/cm}^2$ PTFE membrane.

SMX removal rate. However, the further increased PMS concentration to 2.0 mM led to a slight decrease in SMX removal (95.9%). Excess PMS could deplete part of $\cdot\text{OH}$ and $\text{SO}_4^{\cdot-}$ and produce $\text{SO}_5^{\cdot-}$ with lower oxidizing capacity (Eqs. (1)-(2)) [44]. Besides, self-quenching reactions among excess radicals lead to reduced concentrations (Eqs. (3)-(4)). Therefore, the optimal concentration of PMS was determined as 1.5 mM, which achieved the highest reaction rate constant (k) of 0.1268 min^{-1} .



Afterword, the influence of initial pH on SMX removal was investigated, as shown in Fig. 3(b). In the result, insufficient removal of SMX was observed as the initial pH was 4.5 and 6.5, respectively. About 78.3% and 80.9% of SMX were removed after 60 min with k values of 0.0328 and 0.0356 min^{-1} , respectively (Fig. 3(e)). Whereas the removal rate of SMX increased to 98.9% when the pH was adjusted to 8.6, suggesting that PMS was more prone to be activated under alkaline condition [45]. Additionally, metal catalysts were also difficult to leach at pH 8.6.

In addition, the loading of $\text{CuO}@\text{MnO}_2$ on the PTFE membrane was regarded as the sensitive factor for SMX removal. As shown in Fig. 3(c-f), the k increased gradually with the increase of loading amount of $\text{CuO}@\text{MnO}_2$ from 0.41 to 0.82 mg/cm^2 . The activity reached optimal at a loading of 0.82 mg/cm^2 on the PTFE membrane surface. However, no obvious improvement was observed upon further increasing the loading due to saturation of exposed active sites, smaller pore size, and greater mass transfer resistance [46]. Therefore, the superior loading amount of $\text{CuO}@\text{MnO}_2$ was determined as 0.82 mg/cm^2 for the following reaction system.

Fig. 4 shows SMX degradation in various catalytic systems. The result showed that membrane filtration hardly intercepted SMX without PMS (Fig. 4(a)), owing to the smaller average diameter of SMX ($\sim 1.33 \text{ nm}$) [47] than that of membrane pores. However, SMX concentration started to reduce after adding PMS, demonstrating a crucial role of the oxidation process in the coupled membrane/PMS systems. Further, in the pristine PTFE membrane/PMS system, the SMX removal reached only 67.3%, indicating insufficient degradation of SMX by pure PMS. The removal efficiency of SMX increased slightly in the MnO_2/PTFE membrane/PMS system. Obviously, the MnO_2 was not effective in activating PMS. Comparatively, the removal of SMX could reach 98.9% in the $\text{CuO}@\text{MnO}_2/\text{PTFE}$ membrane/PMS system. The higher removal rate demonstrated that the $\text{CuO}@\text{MnO}_2$ composite could activate PMS sufficiently, hence improving the pollutant removal significantly. Meanwhile, the membrane flux showed no obvious decay in Fig. 4(b),

indicating no contamination of the $\text{CuO}@\text{MnO}_2/\text{PTFE}$ membrane. Additionally, the membrane surface showed hydrophilicity, which can inhibit the adhesion of pollutants effectively.

As shown in Fig. S8 (a), the k value of SMX removal by $\text{CuO}@\text{MnO}_2/\text{PTFE}$ membrane/PMS system was 0.1268 min^{-1} , much higher than that obtained in $\text{CuO}@\text{MnO}_2$ powder/PMS system (0.0949 min^{-1}). In addition, the average flux of the catalytic membrane was $1087 \text{ kg}\cdot\text{m}^{-2}\cdot\text{h}^{-1}$ (Fig. S8 (b)). In this work, the catalytic membrane was fabricated by press-filtering the catalyst on the membrane surface, which exposed fewer active sites compared with the powder catalyst. However, the pollutant removal performance was not decreased compared with that under powder catalyst. It was hypothesized that the nano-confined effect of the bimetal catalyst in the membrane facilitated PMS activation and contaminant removal.

3.2.2. $\text{CuO}@\text{MnO}_2/\text{PTFE}$ membrane stability

Multiple anions and natural organics usually exist in water, which tend to compete for ROS with target contaminants and consequently reduce the removal efficiency of target contaminants. To assess the effects of co-existing substances, NaCl , Na_2SO_4 , NaHCO_3 , NaNO_3 , NaH_2PO_4 and HA were added into the $\text{CuO}@\text{MnO}_2/\text{PTFE}$ membrane/PMS system separately and the results were shown in Fig. 5. No significant effect was observed on SMX removal in the presence of NaCl , Na_2SO_4 , NaHCO_3 , and NaNO_3 (Fig. 5(a)), suggesting that these ions cannot compete with PMS for surface adsorption sites, neither with SMX for ROS. However, H_2PO_4^- exhibited an obvious inhibition, with k value of only 0.0144 min^{-1} (Fig. 5(b)). Besides, the H_2PO_4^- could react with $\text{SO}_4^{\cdot-}$ and $\cdot\text{OH}$ [48]. Also, H_2PO_4^- could form complexes with Cu/Mn on the catalyst surface and inhibit PMS adsorption, hence affecting SMX degradation [48]. HA had a negative effect on SMX removal. The large $\pi\text{-}\pi$ stacking effect facilitated HA adsorption on the active sites of catalysts, eventually preventing the interaction of the catalyst with PMS and SMX [49]. HA also depleted ${}^1\text{O}_2$ and hence affected SMX degradation [50].

In addition, the stability of the $\text{CuO}@\text{MnO}_2/\text{PTFE}$ membrane/PMS system was evaluated by cycling experiments. As shown in Fig. 5(c), the removal rate of SMX was larger than 97% after five cycles, which decreased by only 1.3% compared with the initial filtration, demonstrating the high stability of $\text{CuO}@\text{MnO}_2/\text{PTFE}$ membrane. Besides, there was no leaching of metals in $\text{CuO}@\text{MnO}_2/\text{PTFE}$ membrane/PMS system according to ICP-MS results. The above facts revealed the stability of the system to remove SMX. Furthermore, unlike the traditional powder catalyst, the catalytic membrane did not need to further separate the catalyst after use, which avoided the catalyst loss.

In order to assess the practicality, the $\text{CuO}@\text{MnO}_2/\text{PTFE}$ membrane/PMS system was further applied in the removal of SMX from real wastewater. The wastewater was taken from the secondary effluent of a wastewater treatment plant in Tianjin (China), which contained high concentration of organic matter (COD: $145 \text{ mg}\cdot\text{L}^{-1}$) (Table. S2). To

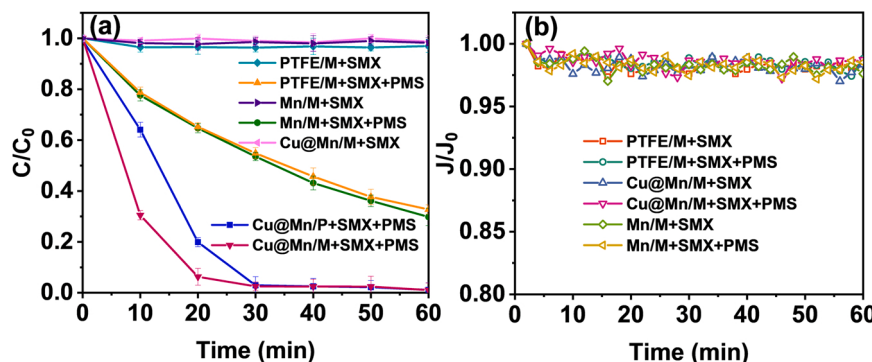


Fig. 4. (a) Removal of SMX and (b) normalized flux in various systems. $C_0(\text{SMX}) = 15 \text{ mg/L}$, $[\text{PMS}] = 1.5 \text{ mM}$, $\text{pH} = 8.6$, $C(\text{CuO}@\text{MnO}_2) = C(\text{MnO}_2) = 0.82 \text{ mg/cm}^2$ PTFE membrane, PTFE/M: PTFE membrane, Mn/M: MnO_2/PTFE membrane, Cu@Mn/M: $\text{CuO}@\text{MnO}_2/\text{PTFE}$ membrane.

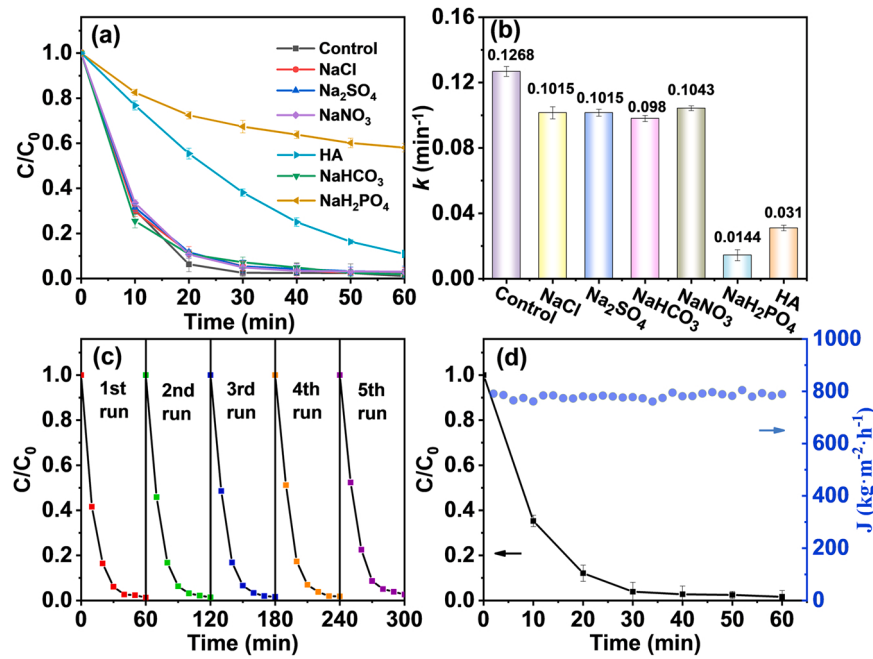


Fig. 5. (a) Effect of aqueous matrix on the removal of SMX in CuO@MnO₂/PTFE membrane/PMS system and (b) corresponding k values; (c) The cycling runs in the CuO@MnO₂/PTFE membrane/PMS system for SMX removal; (d) SMX degradation for secondary effluent. $C_0(\text{SMX}) = 15 \text{ mg/L}$, [PMS] = 1.5 mM, pH = 8.6, $C(\text{CuO@MnO}_2) = 0.82 \text{ mg/cm}^2$ PTFE membrane, [NaCl] = 10 mM, [Na₂SO₄] = 10 mM, [NaNO₃] = 10 mM, [NaHCO₃] = 10 mM, [NaH₂PO₄] = 10 mM, $C(\text{HA}) = 10 \text{ mg/L}$.

simulate the secondary treatment effluent of pharmaceutical wastewater, SMX concentration was added to 15 mg·L⁻¹. The effect of complex aqueous matrix on the removal of SMX was investigated in CuO@MnO₂/PTFE membrane/PMS system with results shown in Fig. 5 (d). Obviously, the CuO@MnO₂/PTFE membrane/PMS system still

effectively removed SMX from the actual wastewater (98.37% within 60 min). Besides, the membrane flux remained stable ($781 \text{ kg}\cdot\text{m}^{-2}\cdot\text{h}^{-1}$) without obvious membrane fouling during the removal process. The above results confirmed the practicality of the CuO@MnO₂/PTFE membrane/PMS system.

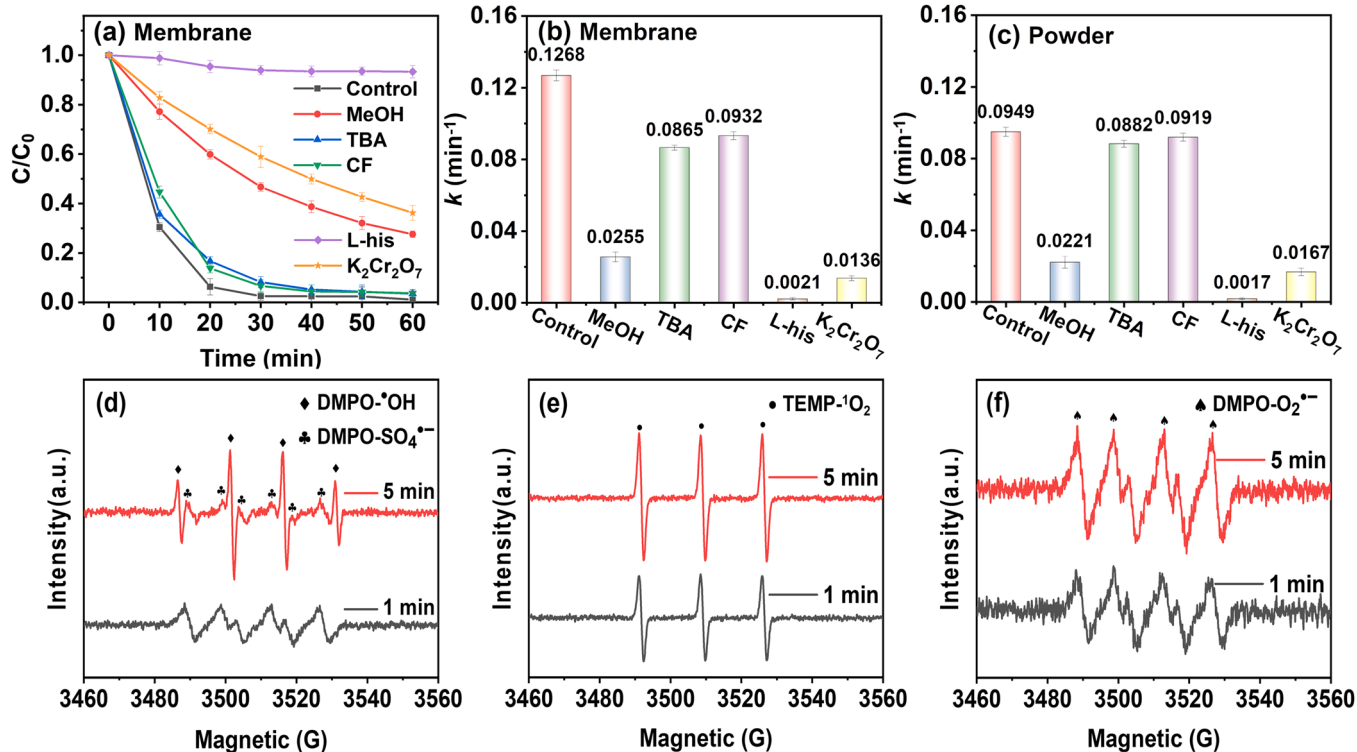


Fig. 6. (a) SMX decomposition with different radical scavengers; The k with different quenchers in (b) CuO@MnO₂/PMS and (c) CuO@MnO₂/PTFE membrane/PMS systems; EPR spectra of (d) DMPO-OH and DMPO-SO₄^{•-}, (e) TEMP-¹O₂, (f) DMPO-O₂^{•-} in CuO@MnO₂/PTFE membrane/PMS system. [MeOH] = [TBA] = 200 mM, [CF] = [L-histidine] = 30 mM, [DMPO] = [TEMP] = 50 mM, [K₂Cr₂O₇] = 10 mM.

3.3. Removal mechanism of SMX in CuO@MnO₂/PTFE membrane/PMS system

3.3.1. Identification of reactive species

The oxidation mechanism of CuO@MnO₂/PTFE membrane/PMS system for the SMX degradation was explored. As shown in Fig. 6, the removal efficiency of SMX was decreased in different degrees as MeOH, TBA, CF, and L-his were added, suggesting that both radical and non-radical pathways were involved in the process of SMX removal (Fig. 6 (a)). Further, the *k* values were calculated under different quenchers in CuO@MnO₂ powder/PMS and CuO@MnO₂/PTFE membrane/PMS systems (Fig. 6(a-b)). It has been proven that SMX carries an electron-donating group and ¹O₂ has unique selectivity and electrophilicity, thus SMX was more easily removed by ¹O₂ [47]. In addition, the electron-rich SMX was difficult to be directly degraded by O₂[•] as O₂[•] is negatively charged. Possibly, O₂[•] might be converted to ¹O₂ to degrade SMX [51,52]. The lowest removal rate of SMX was observed in the presence of L-his. Besides, the removal rate of SMX decreased to 72.4% and 96.5% within 60 min after adding MeOH and TBA in the CuO@MnO₂/PTFE membrane/PMS system, respectively. The above results proved that the •OH, SO₄²⁻ and ¹O₂ played a dominant role in CuO@MnO₂/PTFE membrane/PMS system and CuO@MnO₂ powder/PMS system.

The *k* decreased from 0.1268 to 0.0136 min⁻¹ when 10 mM K₂Cr₂O₇ was added to the CuO@MnO₂/PTFE membrane/PMS system (Fig. 6(b)), indicating the significant contribution of electron transfer to SMX degradation. In addition, the inhibition became stronger in the confined system than in unconfined one, suggesting that the stronger electron transfer between SMX and catalyst-PMS complexes in the confined system (Fig. 6(b) and Fig. 6(c)) [53,54]. Additionally, the i-t curves were further captured the current changes after the addition of PMS and SMX at specific open circuit voltage (Fig. S9). No obvious change of the current was observed after adding PMS, while the current decreased significantly after the introduction of SMX. The coadsorption behavior of PMS and SMX on the surface of Cu-Mn catalysts tends to induce the electron transfer pathway [55,56].

Further, the contribution of different ROSs was estimated via Eqs. (S6-S9) in Text S11 and the results were showed in Fig. S10. Interestingly, the SO₄²⁻ (48.11%) and •OH (31.78%) exhibited an obvious share in CuO@MnO₂/PTFE membrane/PMS system while SO₄²⁻ (69.65%) and ¹O₂ (21.50%) were the main ROSs in CuO@MnO₂/PMS system. Furthermore, the proportion of other ROS such as O₂[•] and high valent metal species (e.g., Mn(IV)) was only 1.66% and 1.79% in both systems, suggesting •OH, SO₄²⁻ and ¹O₂ played a predominant role. The results further demonstrated the differences in PMS activation between CuO@MnO₂/PTFE membrane/PMS system and CuO@MnO₂ /PMS system.

The generation of ROS was further verified by EPR spectroscopy with DMPO and TEMP as spin trapping agents. As demonstrated in Fig. 6(d-f), typical signal peaks of DMPO-•OH (1:2:2:1), DMPO-SO₄²⁻ and DMPO-O₂[•] (sextet line signals) were identified, confirming the presence of •OH, SO₄²⁻ and O₂[•] [40]. Additionally, a triple peak signal (1:1:1) of TEMP-¹O₂ was also detected using TEMP as the ¹O₂ trapping agent. The results were consistent with the quenching experiments. Therefore, •OH, SO₄²⁻, O₂[•] and ¹O₂ could produce through PMS activation by CuO@MnO₂/PTFE membrane, among which SO₄²⁻, •OH and ¹O₂ played major role.

3.3.2. Synergistic mechanism of bimetal in confined environment

Previous studies have summarized that a nano-confined membrane pore size was limited below 25 nm [17]. The membrane pore size distribution of catalytic membranes was tested using Hegselmann-Krause (HK) models of BET (Fig. S11). The pore size of CuO@MnO₂/PTFE and MnO₂/PTFE membranes were in the range of 0.84–2.26 nm. The peak pore sizes of CuO@MnO₂/PTFE and MnO₂/PTFE membranes were 0.84 nm, belonging to the range of nano-confined pore sizes (< 25 nm).

Thus, the nano-confined catalytic effect of CuO@MnO₂/PTFE membrane should be further investigated.

In order to further investigate the interaction between PMS and CuO@MnO₂ in unconfined and confined environment, the adsorption conformation of PMS on CuO@MnO₂ surface was optimized. As shown in Fig. 7, the O-O bond of PMS side-on adsorbed at Cu and Mn atoms of CuO@MnO₂ (O atom with H was adsorbed on Cu atom), respectively (Fig. 7(a) - (c)). The adsorption configuration was more inclined to produce SO₄²⁻ and •OH [57]. Moreover, the adsorption energy of PMS on confined CuO@MnO₂ was -9.02 eV, more negative than unconfined one (-7.84 eV). As a result, the CuO@MnO₂ exhibited higher adsorption ability in confined environment. Moreover, the O-O, S-O and O-H bond lengths were calculated as 1.592 Å, 2.012 Å and 1.053 Å after PMS adsorption on confined CuO@MnO₂ respectively, which were longer than those on unconfined CuO@MnO₂. Thus, PMS was more active at the Cu and Mn sites under confined condition.

In addition, crystal orbital hamilton population (COHP) was calculated to analyze interactions of Cu-O-Mn in confine and unconfine environment before and after PMS adsorption (Fig. 8). Typically, the negative value of the integrated COHP (ICOHP) was positively correlated with the bond energy [22]. As seen from Fig. 8(a-b), the ICOHP of confined Cu-O-Mn was more negative (-1.53) than the unconfined Cu-O-Mn (-1.26). The confined environment enhanced the interaction of Cu and Mn, resulting in stronger electronic coupling. In addition, the d-band centers of the metals might be closer to the Fermi level in confined environment, thereby regulating the electronic distribution, enhancing interactions between Cu and Mn metals and promoting PMS adsorption [13,58]. Previous studies have confirmed the enhanced electronic coupling between metals, which could connect the contaminant and PMS as an electronic bridge. The bridge would reduce the two-step energy barrier from the contaminant to catalyst and from the catalyst to PMS and hence accelerate electron transfer [23]. It can be seen from Fig. 8(c-d) that the electronic coupling of Cu-O-Mn in confined environment was more prone to weakening (-ICOHP = -0.51)

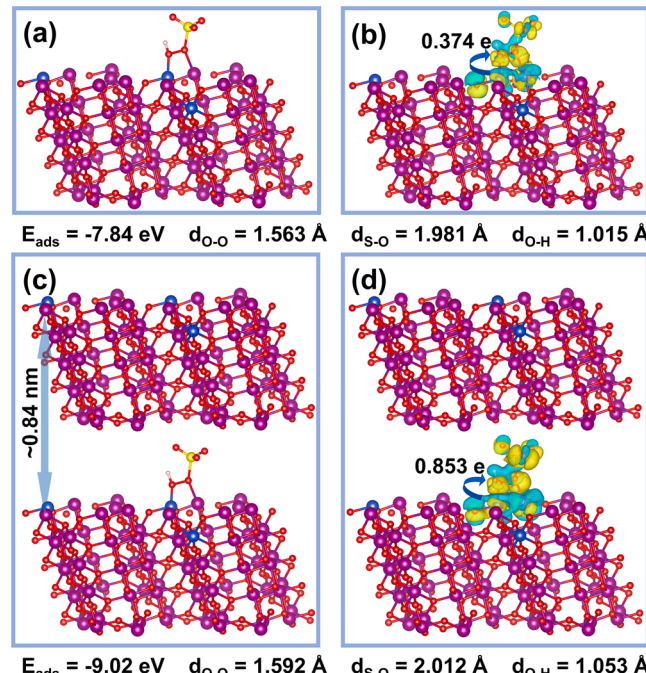


Fig. 7. The optimized adsorption configurations of PMS molecules on the surface of (a) CuO@MnO₂ and (c) CuO@MnO₂/PTFE membrane models. Charge density difference for PMS adsorption on (b) CuO@MnO₂, (d) CuO@MnO₂/PTFE membrane and the corresponding charge transfer. The blue and yellow regions represent the depletion and accumulation of electrons, respectively.

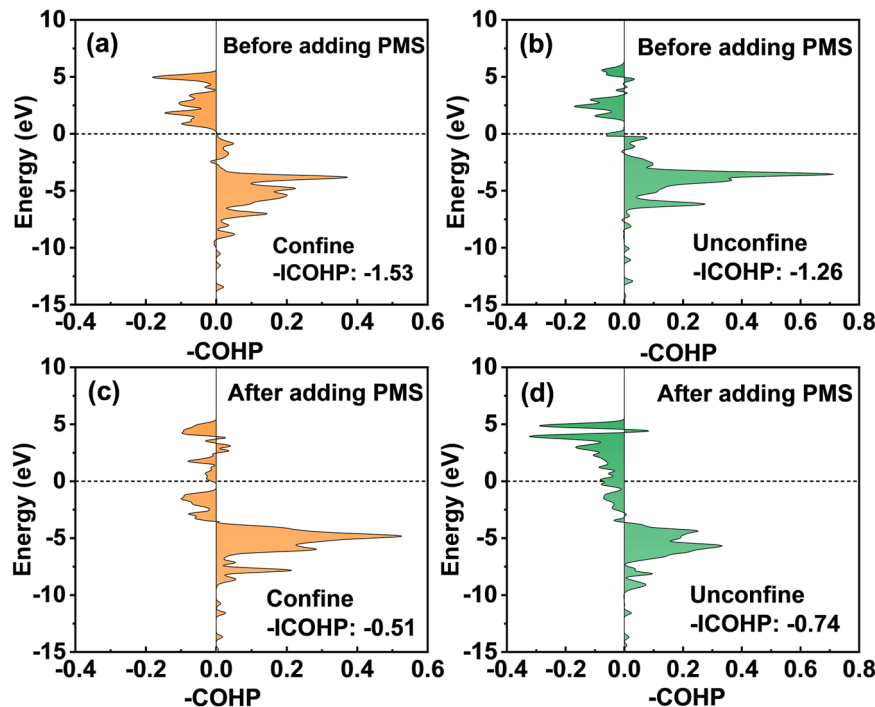


Fig. 8. The COHP of Cu-O-Mn in CuO@MnO₂/PTFE membrane (confine) and CuO@MnO₂ (unconfine) before and after adding PMS.

compared with unconfined (-ICOHP = -0.74) after PMS adsorption. The results confirmed more intensive electron transfer from SMX to PMS under confined environment.

Further, electron distribution in Cu and Mn sites of CuO@MnO₂ under confined and unconfined environment after PMS adsorption was further elucidated via charge density difference. Clearly, the electron depletion occurred at Cu and Mn sites but the electron accumulation was observed at O connected to metals in Fig. 7(b) - (d). In comparison with unconfined CuO@MnO₂, the confined one showed enhanced charge density of Cu and Mn, resulting in a significant improvement of electronic coupling in the electronic bridge between Cu and Mn. Meanwhile, Bader charge calculations demonstrated that the PMS could obtain more electrons from confined CuO@MnO₂ (0.853 e⁻) than unconfined CuO@MnO₂ (0.374 e⁻). The Cu and Mn sites under confined environment achieved efficient adsorption and fast electron transfer to PMS. The above results further confirmed that confined environment could promote electrons enrichment [12,13].

3.3.3. Active sites on CuO@MnO₂/PTFE membrane surface

XPS and FTIR spectra were collected to investigate the changes of surface property before and after the use of CuO@MnO₂/PTFE membrane. As shown in Fig. S12 (a-b), the percentage of Mn(IV) and Mn(III) on the CuO@MnO₂/PTFE membrane surface decreased slightly from 8.56% and 87.84% to 8.54% and 86.95% after use, respectively. Noticeably, the percentage of Mn(II) increased from 3.30% to 4.52%, indicating that different valence states of Mn are involved in PMS activation. In addition, a new peak of Cu(I) appeared on the membrane surface at the binding energy of 935.63 eV after use, while the percentage of Cu(II) decreased from 100% to 51.79%, suggesting the possible presence of redox cycle of Cu(II)/Cu(I) [59]. Notably, the redox potential of Mn(III)/Mn(II) (1.51 V) was higher than that of HSO₅⁻/SO₄²⁻ (1.1 V) but lower than that of HSO₅⁻/SO₄²⁻ (2.5–3.1 V). Therefore, the redox cycle of Mn(III)/Mn(II) was thermodynamically feasible [60]. In addition, the reduction of Mn(IV) and Mn(III) by Cu(I) was thermodynamically feasible according to the greater standard redox potential of Mn(III)/Mn(II) (1.51 V) and Mn

(IV)/Mn(III) (0.95 V) than that of Cu(II)/Cu(I) (0.15 V) [62,63].

Phosphates usually exert an inhibitory effect through strong coordination with transition metals on the catalyst surface [64]. The synergistic effect was reduced when phosphate was added to the reaction system (Fig. 5(a)). This result suggests that phosphate inhibits the synergistic contribution of Cu/Mn, which might be ascribed to the binding of Cu/Mn to phosphate rather than PMS. Thus, the redox cycles of Mn(IV)/Mn(III)/Mn(II) and Cu(II)/Cu(I) were involved in the activation of PMS. And SMX was degraded by the synergistic effect of Cu-Mn bimetal. Besides, the O_{ads}/O_{latt} value of pristine CuO@MnO₂/PTFE membrane (0.91) was higher than that after use (0.67), demonstrating the depletion of O_v in PMS system (Fig. S12 (c)). Moreover, the FTIR spectra (Fig. S12 (d)) exhibited no obvious change after the use of CuO@MnO₂/PTFE membrane, confirming relatively high stability.

Based on the above results, the ROS generation pathway involving Cu and Mn active sites on the surface of CuO@MnO₂/PTFE membrane was proposed (Fig. 9). Orbital optimization of the metals led to electronic rearrangement in the confined environment, which enhanced the electronic coupling between the metals. Further, the orbital changes led to the optimization of the electronic structure of the metal, which was

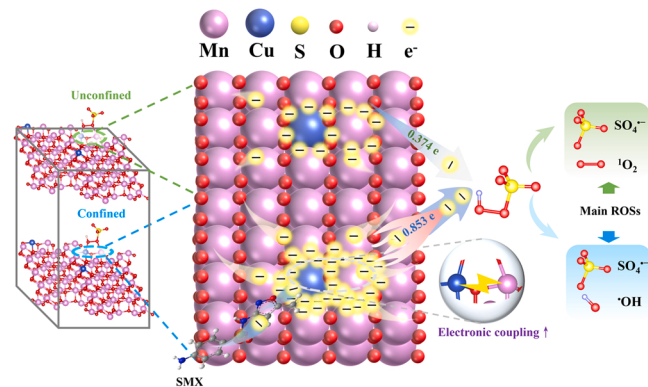


Fig. 9. The mechanism of SMX removal in CuO@MnO₂/PTFE membrane/PMS system.

conducive to the accumulation of electrons. PMS as an electron acceptor was more likely to adsorb to the active site and receive more electrons [65]. In addition, the bimetal acted as an electronic bridge connecting the contaminant to the PMS, resulting in more electrons transferred to the PMS. Ultimately, PMS was rapidly activated to $\cdot\text{OH}$ and $\text{SO}_4^{\cdot-}$, achieving rapid degradation of SMX and reduced toxicity of products (Text 12). Furthermore, redox cycling of metals could promote ROSs generation. First, Mn(II), Mn(III) and Cu(I) reacted with HSO_5^- to form $\text{SO}_4^{\cdot-}$, O_2^- , $\text{SO}_5^{\cdot-}$ and $\cdot\text{OH}$ (Eq. (S10)-(S13)) [66,67]. Meanwhile, PMS was activated by Mn(III), Mn(IV), and Cu(II) to produce $\text{SO}_5^{\cdot-}$ (Eq. (S14)-(S15)) [67]. Additionally, the electrons from SMX were transported to PMS through Cu-O-Mn electronic bridge, and $\text{SO}_5^{\cdot-}$ was produced (Eq. (S16)) [23]. The Cu(I) also reduced Mn(IV) and Mn(III) for electron transfer (Eq. (S17)-(S18)) [68]. Part of $\text{SO}_4^{\cdot-}$ could be converted to $\cdot\text{OH}$ through Eqs. (S19)-(S20). O_2^- could also be further produced from $\text{SO}_5^{\cdot-}$ reaction with H_2O or via self-decomposition of PMS (Eq. (S21)-(S22)). Moreover, O_2^- could also react with $\cdot\text{OH}$ to form O_2 (Eq. (S23)). O_v on the catalyst surface also promoted the conversion of O_{latt} to reactive oxygen species (O^* , like $\text{O}_2^{\cdot-}$ or O^-) and further reacted with PMS to produce O_2 (Eq. (S24)-(S25)) [69]. Eventually, SMX was degraded to intermediates and even partially mineralized by the combination of $\cdot\text{OH}$, $\text{SO}_4^{\cdot-}$, O_2^- and O_2 (Eq. (S26)).

4. Conclusion

In summary, nano-confined $\text{CuO@MnO}_2/\text{PTFE}$ membranes were prepared to activate PMS for SMX oxidation. The $\text{CuO@MnO}_2/\text{PTFE}$ membrane/PMS system exhibited excellent oxidation capacity. In this way, the removal of SMX reached about 98% from actual wastewater within 60 min. Moreover, the stability of the catalytic process was maintained by the Cu/Mn bimetallic redox cycle on the $\text{CuO@MnO}_2/\text{PTFE}$ membrane surface. Additionally, Cu-Mn bimetals in nano-confined membrane promoted PMS activation via enhanced electronic coupling, hence leading to easier adsorption (-9.02 eV) of PMS and more electrons transfer to PMS (0.853 e). The primary ROS were further altered for SMX attack. Main active species of $\text{SO}_4^{\cdot-}$ and O_2^- in an unconfined system ($\text{CuO@MnO}_2/\text{PMS}$ system) were transformed to $\text{SO}_4^{\cdot-}$ and $\cdot\text{OH}$ in a confined one ($\text{CuO@MnO}_2/\text{PTFE}$ membrane/PMS system). Thereby, effective removal of SMX was achieved in the confined system. This study shed a new light on bimetal activation of PMS under nano-confined environment for wastewater treatment.

CRediT authorship contribution statement

Wenjie Gao: Writing – review & editing, Validation, Investigation, Data curation. **Yangli Cui:** Writing – review & editing, Writing – original draft, Validation, Methodology, Investigation, Formal analysis, Conceptualization. **Eslam Salama:** Writing – review & editing, Visualization. **Wenchao Peng:** Writing – review & editing, Investigation, Formal analysis. **Ning Li:** Writing – review & editing, Supervision, Project administration, Funding acquisition. **Beibei Yan:** Writing – review & editing. **Guanyi Chen:** Writing – review & editing, Supervision. **Mona Ossman:** Writing – review & editing, Visualization, Investigation. **Xu He:** Writing – review & editing, Investigation. **Lan Liang:** Writing – review & editing, Visualization, Investigation.

Declaration of Competing Interest

The authors declare that they have no known competing financial interests or personal relationships that could have appeared to influence the work reported in this paper.

Data availability

Data will be made available on request.

Acknowledgements

This work was supported by National Natural Science Foundation of China (No. 52100156), Shenzhen Science and Technology Program (No. GJHZ20200731095801005, JCYJ20200109150210400), and Tianjin Science and Technology Planning Project (No. 21JCQNJC00400).

Appendix A. Supporting information

Supplementary data associated with this article can be found in the online version at doi:10.1016/j.apcatb.2024.123955.

References

- [1] A.J. Kang, A.K. Brown, C.S. Wong, Q. Yuan, Removal of antibiotic sulfamethoxazole by anoxic/anaerobic/oxic granular and suspended activated sludge processes, *Bioresour. Technol.* 251 (2018) 151–157, <https://doi.org/10.1016/j.biortech.2017.12.021>.
- [2] D. Hu, H. Min, H. Wang, Y. Zhao, Y. Cui, P. Wu, H. Ge, K. Luo, L. Zhang, W. Liu, A. Wang, Performance of an up-flow anaerobic bio-electrochemical system (UBES) for treating sulfamethoxazole (SMX) antibiotic wastewater, *Bioresour. Technol.* 305 (2020) 123070, <https://doi.org/10.1016/j.biortech.2020.123070>.
- [3] A.S. Oberoi, Y. Jia, H. Zhang, S.K. Khanal, H. Lu, Insights into the fate and removal of antibiotics in engineered biological treatment systems: a critical review, *Environ. Sci. Technol.* 53 (2019) 7234–7264, <https://doi.org/10.1021/acs.est.9b01131>.
- [4] Z. Huang, P. Wu, C. Liu, M. Chen, S. Yang, Z. Dang, N. Zhu, Multiple catalytic reaction sites induced non-radical/radical pathway with graphene layers encapsulated Fe-N-C toward highly efficient peroxyomonosulfate (PMS) activation, *Chem. Eng. J.* 413 (2021) 127507, <https://doi.org/10.1016/j.cej.2020.127507>.
- [5] M. Kohantorabi, G. Moussavi, S. Giannakis, A review of the innovations in metal- and carbon-based catalysts explored for heterogeneous peroxyomonosulfate (PMS) activation, with focus on radical vs. non-radical degradation pathways of organic contaminants, *Chem. Eng. J.* 411 (2021) 127957, <https://doi.org/10.1016/j.cej.2020.127957>.
- [6] X. Zheng, X. Niu, D. Zhang, M. Lv, X. Ye, J. Ma, Z. Lin, M. Fu, Metal-based catalysts for persulfate and peroxyomonosulfate activation in heterogeneous ways: a review, *Chem. Eng. J.* 429 (2022) 132323, <https://doi.org/10.1016/j.cej.2021.132323>.
- [7] Y. Ding, L. Fu, X. Peng, M. Lei, C. Wang, J. Jiang, Copper catalysts for radical and nonradical persulfate based advanced oxidation processes: Certainties and uncertainties, *Chem. Eng. J.* 427 (2022) 131776, <https://doi.org/10.1016/j.cej.2021.131776>.
- [8] J. Huang, H. Zhang, Mn-based catalysts for sulfate radical-based advanced oxidation processes: a review, *Environ. Int.* 133 (2019) 105141, <https://doi.org/10.1016/j.envint.2019.105141>.
- [9] J. Wei, F. Li, L. Zhou, D. Han, J. Gong, Strategies for enhancing peroxyomonosulfate activation by heterogeneous metal-based catalysis: a review, *Chin. J. Chem. Eng.* 50 (2022) 12–28, <https://doi.org/10.1016/j.cjche.2022.07.032>.
- [10] J. Zhang, W. Zhao, S. Wu, R. Yin, M. Zhu, Surface dual redox cycles of Mn(III)/Mn(IV) and Cu(II)/Cu(II) for heterogeneous peroxyomonosulfate activation to degrade diclofenac: performance, mechanism and toxicity assessment, *J. Hazard. Mater.* 410 (2021) 124623, <https://doi.org/10.1016/j.jhazmat.2020.124623>.
- [11] Z. Zhu, X. Yu, J. Qu, Y. Jing, Y. Abdelkrim, Z. Yu, Preforming abundant surface cobalt hydroxyl groups on low crystalline flowerlike $\text{Co}_3(\text{Si}_2\text{O}_5)_2(\text{OH})_2$ for enhancing catalytic degradation performances with a critical nonradical reaction, *Appl. Catal. B: Environ.* 261 (2020) 118238, <https://doi.org/10.1016/j.apcatb.2019.118238>.
- [12] F. Wang, Y. Gao, H. Fu, S.S. Liu, Y. Wei, P. Wang, C. Zhao, J.F. Wang, C.C. Wang, Almost 100% electron transfer regime over Fe–Co dual-atom catalyst toward pollutants removal: regulation of peroxyomonosulfate adsorption mode, *Appl. Catal. B: Environ.* 339 (2023) 123178, <https://doi.org/10.1016/j.apcatb.2023.123178>.
- [13] F. Wang, Y. Gao, H. Chu, Y. Wei, C.C. Wang, S.S. Liu, G. Liu, H. Fu, P. Wang, C. Zhao, The pivotal role of selenium vacancies in defective $\text{FeSe}_2/\text{MoO}_3$ for efficient peroxyomonosulfate activation: experimental and DFT calculation, *ACS EST Eng.* (2023), <https://doi.org/10.1021/acsestengg.3c00195>.
- [14] Z. Xie, D.D. Dionysiou, S. Luo, M. Chen, Z. Wei, Dual-reaction center catalyst based on common metals Cu-Mg-Al for synergistic peroxyomonosulfate adsorption-activation in Fenton-like process, *Appl. Catal. B: Environ.* 327 (2023) 122468, <https://doi.org/10.1016/j.apcatb.2023.122468>.
- [15] J. Qian, X. Gao, B. Pan, Nanoconfinement-mediated water treatment: From fundamental to application, *Environ. Sci. Technol.* 54 (2020) 8509–8526, <https://doi.org/10.1021/acs.est.0c01065>.
- [16] S. Zhang, T. Hedtke, Q. Zhu, M. Sun, S. Weon, Y. Zhao, E. Stavitski, M. Elimelech, J.-H. Kim, Membrane-confined iron oxychloride nanocatalysts for highly efficient heterogeneous fenton water treatment, *Environ. Sci. Technol.* 55 (2021) 9266–9275, <https://doi.org/10.1021/acs.est.1c01391>.
- [17] Q.V. Ly, L. Cui, M.B. Asif, W. Khan, L.D. Nghiem, Y. Hwang, Z. Zhang, Membrane-based nanoconfined heterogeneous catalysis for water purification: a critical review, *Water Res.* 230 (2023) 119577, <https://doi.org/10.1016/j.watres.2023.119577>.

- [18] M.B. Asif, S. Zhang, L. Qiu, Z. Zhang, Ultrahigh-permeance functionalized boron nitride membrane for nanoconfined heterogeneous catalysis, *Chem. Catal.* 2 (2022) 550–562, <https://doi.org/10.1016/j.cheat.2022.01.003>.
- [19] W. Zhang, S. Zhang, Z. Chen, Z. Zhang, Cobalt-ferrite functionalized graphitic carbon nitride ($\text{CoFe}_2\text{O}_4@\text{g-C}_3\text{N}_4$) nanoconfined catalytic membranes for efficient water purification: performance and mechanism, *J. Mater. Chem. A* 11 (2023) 18933–18944, <https://doi.org/10.1039/D3TA03247G>.
- [20] M. Tang, J. Wan, Y. Wang, G. Ye, Z. Yan, Y. Ma, J. Sun, Overlooked role of void-nanoconfined effect in emerging pollutant degradation: modulating the electronic structure of active sites to accelerate catalytic oxidation, *Water Res.* 249 (2024) 120950, <https://doi.org/10.1016/j.watres.2023.120950>.
- [21] X. Li, X.I. Pereira-Hernández, Y. Chen, J. Xu, J. Zhao, C.-W. Pao, C.-Y. Fang, J. Zeng, Y. Wang, B.C. Gates, J. Liu, Functional CeO_x nanogels for robust atomically dispersed catalysts, *Nature* 611 (2022) 284–288, <https://doi.org/10.1038/s41586-022-05251-6>.
- [22] X. Zhang, J. Liu, H. Zhang, Z. Wan, J. Li, Uncovering the pathway of peroxymonosulfate activation over $\text{Co}_{0.5}\text{Zn}_{0.5}\text{O}$ nanosheets for singlet oxygen generation: performance and membrane application, *Appl. Catal. B: Environ.* 327 (2023) 122429, <https://doi.org/10.1016/j.apcatb.2023.122429>.
- [23] J. Xu, Y. Yao, C. Zhu, L. Lu, Q. Fang, Z. He, S. Song, B. Chen, Y. Shen, Unveiling enhanced electron-mediated peroxymonosulfate activation for degradation of emerging organic pollutants, *Appl. Catal. B: Environ.* 341 (2024) 123356, <https://doi.org/10.1016/j.apcatb.2023.123356>.
- [24] X. Zhai, L. Li, S. Song, J. Zhang, J. Ma, C. Xie, W. Chu, Influence of MnO_2 crystal existing form on its catalytic performance for toluene oxidation, *Fuel* 334 (2023) 126780, <https://doi.org/10.1016/j.fuel.2022.126780>.
- [25] X. Ren, P. Xu, K. Tian, M. Cao, F. Shi, G. Zhang, Peroxymonosulfate activation by $\text{CuO}-\text{Fe}_2\text{O}_3$ -modified Ni foam: A ^1O_2 dominated process for efficient and stable degradation of tetracycline, *Catalysts* 13 (2023) 329, <https://doi.org/10.3390/catal13020329>.
- [26] S. Chen, F. Liu, R. Cui, B. Zhu, X. You, Removal of tetracycline hydrochloride using $\text{S}-\text{g-C}_3\text{N}_4/\text{PTFE}$ membrane under visible light irradiation, *Water Cycle* 3 (2022) 8–17, <https://doi.org/10.1016/j.watcyc.2022.01.001>.
- [27] E.A. Arkhipova, A.S. Ivanov, K.I. Maslakov, R.Y. Novotortsev, S.V. Savilov, H. Xia, A.V. Desyatov, S.M. Aldoshin, Facile hydrothermal synthesis of $\alpha\text{-MnO}_2$ and $\delta\text{-MnO}_2$ for pseudocapacitor applications, *Ionics* 28 (2022) 3501–3509, <https://doi.org/10.1007/s11581-022-04562-y>.
- [28] M.A. Stranick, MnO_2 by XPS, *Surf. Sci. Spectra* 6 (1999) 31–38, <https://doi.org/10.1116/1.1247888>.
- [29] T. Matthew, K. Suzuki, Y. Ikuta, N. Takahashi, H. Shinjoh, Mesoporous ferrihydrite with incorporated manganese for rapid removal of organic contaminants in air, *Chem. Commun.* 48 (2012) 10987–10989, <https://doi.org/10.1039/C2CC36120E>.
- [30] Y. Sun, X. Wang, Y. Dong, X. Niu, Y. Zhu, Enhanced low-temperature catalytic combustion of toluene over Cu and Mn co-modified $\alpha\text{-MnO}_2$ with flower spheres, *J. Environ. Chem. Eng.* 11 (2023) 110670, <https://doi.org/10.1016/j.jece.2023.110670>.
- [31] Y. Huang, X. Tian, Y. Nie, C. Yang, Y. Wang, Enhanced peroxymonosulfate activation for phenol degradation over MnO_2 at pH 3.5–9.0 via Cu(II) substitution, *J. Hazard. Mater.* 360 (2018) 303–310, <https://doi.org/10.1016/j.jhazmat.2018.08.028>.
- [32] J. Zhang, H. Zhang, X. Zhu, H. Liu, G. Hou, H. Kang, B. Liu, W. Zhu, S. Yin, Z. Song, Constructing three-dimensional Mn_2O_3 catalysts with various morphologies for catalytic oxidation of benzene, *Appl. Organomet. Chem.* 37 (2023) e7010, <https://doi.org/10.1002/aoc.7010>.
- [33] Y. Ding, C. Pan, X. Peng, Q. Mao, Y. Xiao, L. Fu, J. Huang, Deep mineralization of bisphenol A by catalytic peroxymonosulfate activation with nano $\text{CuO}/\text{Fe}_3\text{O}_4$ with strong Cu–Fe interaction, *Chem. Eng. J.* 384 (2020) 123378, <https://doi.org/10.1016/j.cej.2019.123378>.
- [34] M. Wang, C. Jin, J. Kang, J. Liu, Y. Tang, Z. Li, S. Li, $\text{CuO/g-C}_3\text{N}_4$ 2D/2D heterojunction photocatalysts as efficient peroxymonosulfate activators under visible light for oxytetracycline degradation: characterization, efficiency and mechanism, *Chem. Eng. J.* 416 (2021) 128118, <https://doi.org/10.1016/j.cej.2020.128118>.
- [35] J. Wang, J. Fan, J. Yao, X. Wu, C. Gao, Z. Wei, Y. Li, Facet tailoring and Cu doping promoted photo-assisted peroxymonosulfate activation by oxygen-deficient $\alpha\text{-MnO}_2$ for efficient mineralization of bisphenol a, *Chem. Eng. J.* 461 (2023) 142024, <https://doi.org/10.1016/j.cej.2023.142024>.
- [36] H. Zhao, X. Liu, Y. Liu, D. Wu, W. Hu, X. Shang, M. Lv, Directionally inducing non-radical pathways for peroxymonosulfate activation by regulating the exposed crystal plane of MnO_2 , *Process Saf. Environ. Prot.* 177 (2023) 947–958, <https://doi.org/10.1016/j.psep.2023.07.038>.
- [37] H. Yi, Y. Wang, L. Diao, Y. Xin, C. Chai, D. Cui, D. Ma, Ultrasonic treatment enhances the formation of oxygen vacancies and trivalent manganese on $\alpha\text{-MnO}_2$ surfaces: Mechanism and application, *J. Colloid Interface Sci.* 626 (2022) 629–638, <https://doi.org/10.1016/j.jcis.2022.06.144>.
- [38] W. Ruan, S. Shi, Q. Wang, X. Zhang, W. Hao, C. Yuan, B. Ma, G. Cheng, F. Teng, Innovative electrolytic cell of sulfur-doped MnO_2 nanorods: Synergistic hydrogen production and formaldehyde degradation at an ultra-low electric energy consumption, *J. Alloy. Compd.* 925 (2022) 166748, <https://doi.org/10.1016/j.jallcom.2022.166748>.
- [39] X. Chen, Y. Li, Y. Yang, D. Zhang, Y. Guan, M. Bao, Z. Wang, A super-hydrophobic and antibiofouling membrane constructed from carbon sphere-welded MnO_2 nanowires for ultra-fast separation of emulsion, *J. Membr. Sci.* 653 (2022) 120514, <https://doi.org/10.1016/j.memsci.2022.120514>.
- [40] J. Sun, D. Zhang, D. Xia, Q. Li, Orange peels biochar doping with Fe–Cu bimetal for PMS activation on the degradation of Bisphenol A: a synergy of SO_4^{2-} , $\cdot\text{OH}$, ^1O_2 and electron transfer, *Chem. Eng. J.* 471 (2023) 144832, <https://doi.org/10.1016/j.cej.2023.144832>.
- [41] X. Zhou, L. Zhang, H. Wang, W. Lu, R. Zhang, H. Li, J. Li, X. Wei, The regulation of generation rate facilitates the win-win of ROS yield and utilization efficiency in heterogeneous persulfate catalytic oxidation system, *Sep. Purif. Technol.* 323 (2023) 124389, <https://doi.org/10.1016/j.seppur.2023.124389>.
- [42] J. Piwowarczyk, R. Jędrzejewski, D. Moszyński, K. Kwiatkowski, A. Niemczyk, J. Baranowska, XPS and FTIR studies of polytetrafluoroethylene thin films obtained by physical methods, *Polymers* (2019).
- [43] M.A. Saffar, A. Eshagh, M.R. Dehnavi, Fabrication of superhydrophobic, self-cleaning and anti-icing $\text{ZnO}/\text{PTFE-SiO}_2$ nano-composite thin film, *Mater. Chem. Phys.* 259 (2021) 124085, <https://doi.org/10.1016/j.matchemphys.2020.124085>.
- [44] J. Ye, J. Dai, C. Li, Y. Yan, Lawn-like Co_3O_4 @N-doped carbon-based catalytic self-cleaning membrane with peroxyxonosulfate activation: a highly efficient singlet oxygen dominated process for sulfamethoxazole degradation, *Chem. Eng. J.* 421 (2021) 127805, <https://doi.org/10.1016/j.cej.2020.127805>.
- [45] X. Zhu, L. Ge, W. Yan, S. Yang, G. Wang, D. Miao, P. Jin, Peroxyxonosulfate activation by immobilized CoFe_2O_4 network for the degradation of sulfamethoxazole, *J. Environ. Chem. Eng.* 10 (2022) 107781, <https://doi.org/10.1016/j.jece.2022.107781>.
- [46] H. Ma, G. Wang, Z. Miao, X. Dong, X. Zhang, Integration of membrane filtration and peroxyxonosulfate activation on CNT@nitrogen doped carbon/ Al_2O_3 membrane for enhanced water treatment: insight into the synergistic mechanism, *Sep. Purif. Technol.* 252 (2020) 117479, <https://doi.org/10.1016/j.seppur.2020.117479>.
- [47] H. Ma, X. Li, Z. Pan, R. Xu, P. Wang, H. Li, Y. Shi, X. Fan, C. Song, MOF derivative functionalized titanium-based catalytic membrane for efficient sulfamethoxazole removal via peroxyxonosulfate activation, *J. Membr. Sci.* 661 (2022) 120924, <https://doi.org/10.1016/j.memsci.2022.120924>.
- [48] W. Oh, Z. Dong, T.T. Lim, Generation of sulfate radical through heterogeneous catalysis for organic contaminants removal: current development, challenges and prospects, *Appl. Catal. B: Environ.* 194 (2016) 169–201, <https://doi.org/10.1016/j.apcatb.2016.04.003>.
- [49] X. Yang, F.L. Rosario Ortiz, Y. Lei, Y. Pan, X. Lei, P. Westerhoff, Multiple roles of dissolved organic matter in advanced oxidation processes, *Environ. Sci. Technol.* 56 (2022) 11111–11131, <https://doi.org/10.1021/acs.est.2c01017>.
- [50] L.S. Zhang, X.H. Jiang, Z.A. Zhong, L. Tian, Q. Sun, Y.T. Cui, X. Lu, J.P. Zou, S. L. Luo, Carbon nitrile supported high-loading Fe single-atom catalyst for activation of peroxyxonosulfate to generate ^1O_2 with 100% selectivity, *Angew. Chem. Int. Ed.* 60 (2021) 21751–21755, <https://doi.org/10.1002/anie.202109488>.
- [51] J. Cheng, S. Wan, S. Cao, Promoting solar-driven hydrogen peroxide production over thiiazole-based conjugated polymers via generating and converting singlet oxygen, *Angew. Chem. Int. Ed.* 62 (2023) e202310476, <https://doi.org/10.1002/anie.202310476>.
- [52] Q. Yi, J. Ji, B. Shen, C. Dong, J. Liu, J. Zhang, M. Xing, Singlet oxygen triggered by superoxide radicals in a molybdenum cocatalytic fenton reaction with enhanced redox activity in the environment, *Environ. Sci. Technol.* 53 (2019) 9725–9733, <https://doi.org/10.1021/acs.est.9b01676>.
- [53] X. Guo, H. Zhang, Y. Yao, C. Xiao, X. Yan, K. Chen, J. Qi, Y. Zhou, Z. Zhu, X. Sun, J. Li, Derivatives of two-dimensional MXene-MOFs heterostructure for boosting peroxyxonosulfate activation: enhanced performance and synergistic mechanism, *Appl. Catal. B: Environ.* 323 (2023) 122136, <https://doi.org/10.1016/j.apcatb.2022.122136>.
- [54] F. Qin, E. Almatrafi, C. Zhang, D. Huang, L. Tang, A. Duan, D. Qin, H. Luo, C. Zhou, G. Zeng, Catalyst-free photochemical activation of peroxyxonosulfate in xanthene-rich systems for fenton-like synergistic decontamination: efficacy of proton transfer process, *Angew. Chem. Int. Ed.* 62 (2023) e202300256, <https://doi.org/10.1002/anie.202300256>.
- [55] C. Zhao, L. Meng, H. Chu, J.-F. Wang, T. Wang, Y. Ma, C.-C. Wang, Ultrafast degradation of emerging organic pollutants via activation of peroxyxonosulfate over $\text{Fe}_3\text{O}_4/\text{Fe-N-C-x}$: singlet oxygen evolution and electron-transfer mechanisms, *Appl. Catal. B: Environ.* 321 (2023) 122034, <https://doi.org/10.1016/j.apcatb.2022.122034>.
- [56] W. Li, L. Jin, S. Jiang, Y. Liu, Electrified nitrogen-doped MXene membrane electrode for micropollutants decontamination via peroxyxonosulfate activation, *ACS EST Eng.* 4 (2024) 176–185, <https://doi.org/10.1021/acsesestengg.3c00222>.
- [57] Z. Zhao, P. Wang, C. Song, T. Zhang, S. Zhan, Y. Li, Enhanced interfacial electron transfer by asymmetric $\text{Cu-O}_x-\text{Li}$ sites on In_2O_3 for efficient peroxyxonosulfate activation, *Angew. Chem. (Int. Ed. Engl.)* 62 (2023) e202216403, <https://doi.org/10.1002/anie.202216403>.
- [58] L. Zhao, Q. Cai, B. Mao, J. Mao, H. Dong, Z. Xiang, J. Zhu, R. Paul, D. Wang, Y. Long, L. Qu, R. Yan, L. Dai, C. Hu, A universal approach to dual-metal-atom catalytic sites confined in carbon dots for various target reactions, *Proc. Natl. Acad. Sci.* 120 (2023) e2308828120, <https://doi.org/10.1073/pnas.2308828120>.
- [59] L. Liu, C. Han, G. Ding, M. Yu, Y. Li, S. Liu, Y. Xie, J. Liu, Oxygen vacancies-enriched Cu/Co bimetallic oxides catalysts for high-efficiency peroxyxonosulfate activation to degrade TC: insight into the increase of Cu^+ triggered by Co doping, *Chem. Eng. J.* 450 (2022) 138302, <https://doi.org/10.1016/j.cej.2022.138302>.
- [60] G. Huang, C. Wang, C. Yang, P. Guo, H. Yu, Degradation of bisphenol A by peroxyxonosulfate catalytically activated with $\text{Mn}_{1.8}\text{Fe}_{1.2}\text{O}_4$ nanospheres: synergism between Mn and Fe, *Environ. Sci. Technol.* 51 (2017) 12611–12618, <https://doi.org/10.1021/acs.est.7b03007>.
- [61] L. Wang, H. Xu, N. Jiang, Z. Wang, J. Jiang, T. Zhang, Trace cupric species triggered decomposition of peroxyxonosulfate and degradation of organic pollutants: Cu(III) being the primary and selective intermediate oxidant, *Environ. Sci. Technol.* 54 (2020) 4686–4694, <https://doi.org/10.1021/acs.est.0c00284>.

- [62] G. Cai, Y. Tian, D. Li, J. Zhang, L. Li, Q. Wang, H. Sun, H. Zhang, P. Wang, Self-enhanced and efficient removal of As(III) from water using Fe–Cu–Mn composite oxide under visible-light irradiation: Synergistic oxidation and mechanisms, *J. Hazard. Mater.* 422 (2022) 126908, <https://doi.org/10.1016/j.jhazmat.2021.126908>.
- [63] M. Zhang, A. Cao, H. Zhang, C. Yang, Defective MNiFeO ($M = Cu, Zn, Co, Mn$) NRs derived from cation-exchanged Fe_2Ni -MOFs for catalytic nitroarene hydrogenation, *J. Colloid Interface Sci.* 623 (2022) 63–76, <https://doi.org/10.1016/j.jcis.2022.04.177>.
- [64] T. Zhang, C. Li, J. Ma, H. Tian, Z. Qiang, Surface hydroxyl groups of synthetic α -FeOOH in promoting $^{\bullet}OH$ generation from aqueous ozone: property and activity relationship, *Appl. Catal. B: Environ.* 82 (2008) 131–137, <https://doi.org/10.1016/j.apcatb.2008.01.008>.
- [65] Z. Weng, Y. Lin, S. Guo, X. Zhang, Q. Guo, Y. Luo, X. Ou, J. Ma, Y. Zhou, J. Jiang, B. Han, Site engineering of covalent organic frameworks for regulating peroxyomonosulfate activation to generate singlet oxygen with 100% Selectivity, *Angew. Chem. Int. Ed.* 62 (2023) e202310934, <https://doi.org/10.1002/anie.202310934>.
- [66] J. Shang, T. Zhang, X. Li, Y. Luo, D. Feng, X. Cheng, Mn_3O_4 – $ZnMn_2O_4$ /SnO₂ nanocomposite activated peroxyomonosulfate for efficient degradation of ciprofloxacin in water, *Sep. Purif. Technol.* 311 (2023) 123342, <https://doi.org/10.1016/j.seppur.2023.123342>.
- [67] J. Du, J. Bao, Y. Liu, S.H. Kim, D.D. Dionysiou, Facile preparation of porous Mn/Fe₃O₄ cubes as peroxyomonosulfate activating catalyst for effective bisphenol A degradation, *Chem. Eng. J.* 376 (2019) 119193, <https://doi.org/10.1016/j.cej.2018.05.177>.
- [68] B. Chen, J. Wang, R. Li, H. Lin, B. Li, L. Shen, Y. Xu, M. Zhang, Fabrication of CoFe₂O₄/Mn₃O₄ decorated ultrathin graphitic carbon nitride nanosheets membrane for persistent organic pollutants removal: Synergistic performance and mechanisms, *Sep. Purif. Technol.* 309 (2023) 123076, <https://doi.org/10.1016/j.seppur.2022.123076>.
- [69] H. Chen, Y. Xu, K. Zhu, H. Zhang, Understanding oxygen-deficient La₂CuO₄-perovskite activated peroxyomonosulfate for bisphenol A degradation: the role of localized electron within oxygen vacancy, *Appl. Catal. B: Environ.* 284 (2021) 119732, <https://doi.org/10.1016/j.apcatb.2020.119732>.